ACS NANO

www.acsnano.org

ARTICLE

Ferroelectrically Modulated and Enhanced Photoresponse in a Self-Powered α-In_2Se_3/Si Heterojunction Photodetector

Cheng Jia,* Shuangxiang Wu, Jinze Fan, Chaojie Luo, Minghui Fan, Ming Li, Lanping He, Yuanjun Yang,* and Hui Zhang*

Cite This: *ACS Nano* 2023, 17, 6534−6544

Read Online

ACCESS | Metrics & More | Article Recommendations | Supporting Information

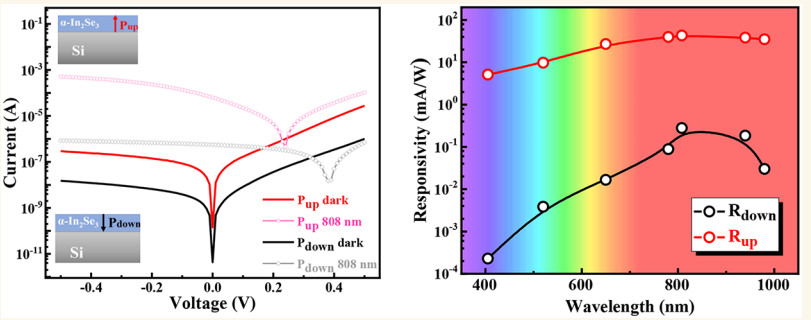

ABSTRACT: Photodetectors have been applied to pivotal optoelectronic components of modern optical communication, sensing, and imaging systems. As a room-temperature ferroelectric van der Waals semiconductor, 2D α-In_2Se_3 is a promising candidate for a next-generation optoelectronic material because of its thickness-dependent direct bandgap and excellent optoelectronic performance. Previous studies of photodetectors based on α-In_2Se_3 have been rarely focused on the modulated relationship between the α-In_2Se_3 intrinsic ferroelectricity and photoresponsivity. Herein, a simple integrated process and high-performance photodetector based on an α-In_2Se_3/Si vertical hybrid-dimensional heterojunction was constructed. Our photodetector in the ferroelectric polarization up state accomplishes a self-powered, highly sensitive photoresponse with an on/off ratio of 4.5×10^5 and detectivity of 1.6×10^{13} Jones, and it also shows a fast response time with 43 μs. The depolarization field generated by the remanent polarization of ferroelectrics in α-In_2Se_3 provides a strategy for enhancement and modulation of photodetection. The negative correlation was discovered because the enhancement photoresponsivity factor of ferroelectric modulation competes with the photovoltaic behavior within the α-In_2Se_3/Si heterojunction. Our research highlights the great potential of the high-efficiency heterojunction photodetector for future object recognition and photoelectric imaging.

KEYWORDS: *Photodetector, 2D Ferroelectric Materials, α-In_2Se_3, Heterojunction, NIR Imaging*

1. INTRODUCTION

Photodetectors are critical components in optoelectronic integrated circuits such as optoelectronic sensors, space research, imaging systems, and optical switching logic devices.[1−8] The constituent materials of the targeted devices determine the working mechanism and performances of photodetectors.[9,10] In view of two-dimensional (2D) materials' superior performance and fascinating physics, emerging devices based on 2D materials and their hybrid systems have been developed recently in contrast to conventional semiconductor-based photodetectors.[11−15] Without surface dangling bonds and intralayer covalent bonding as well as interlayer van der Waals (vdW) interactions, 2D materials can be used to design a variety of vdW heterostructures and are compatible with silicon-based optoelectronic technologies.[1,2,15]

To improve the performance of 2D photodetectors, various modulated methods have emerged, such as the construction of

Received: November 30, 2022
Accepted: February 8, 2023
Published: March 23, 2023

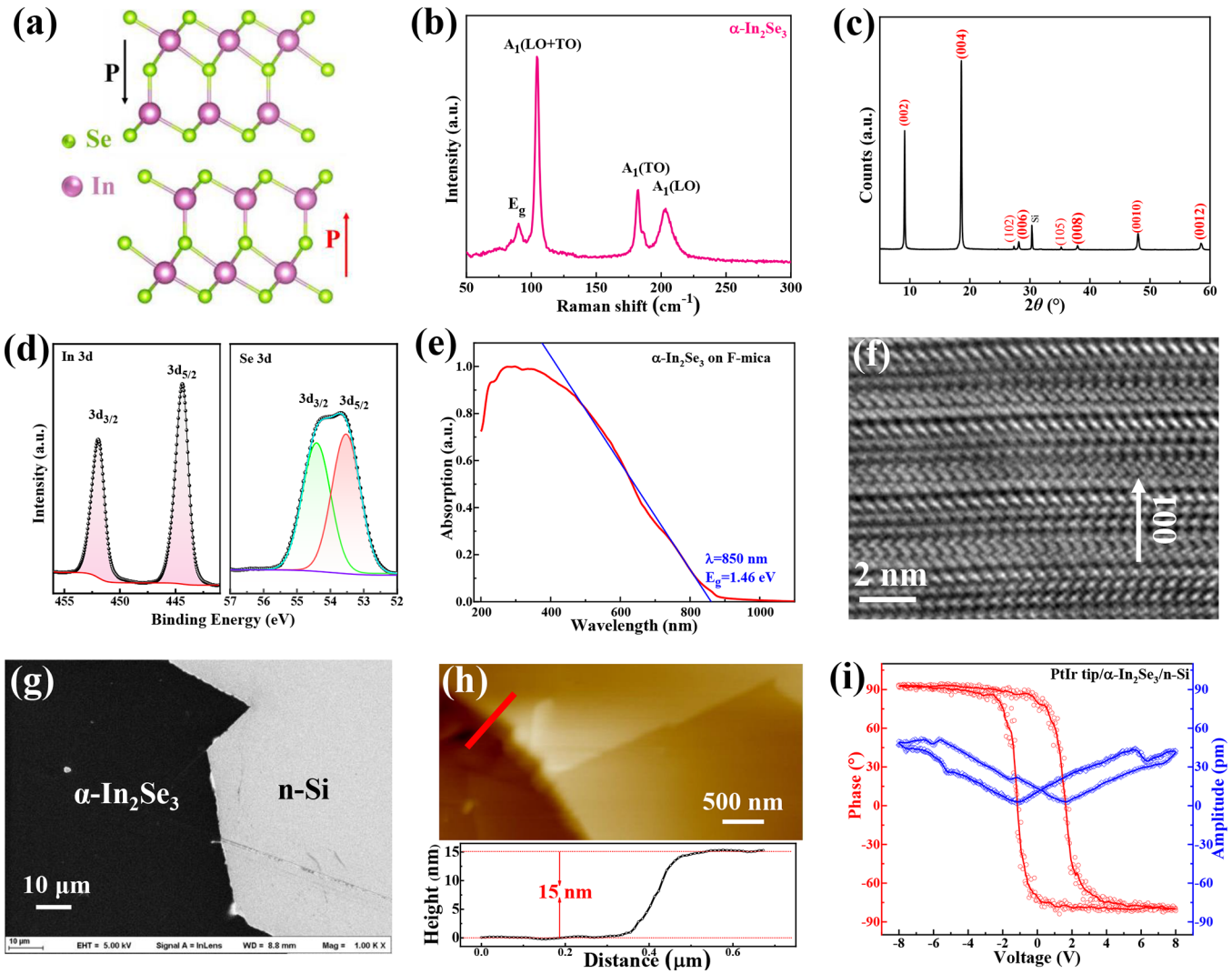

Figure 1. Characterizations of α-In_2Se_3 film. (a) Crystal structure side view of 2D ($P_{up/down}$ states) layered α-In_2Se_3. (b) Raman spectra of the α-In_2Se_3. (c) XRD patterns of the transferred α-In_2Se_3 film on Si substrate. (d) XPS spectra of the In 3d and Se 3d. (e) Absorption spectrum of the α-In_2Se_3 film. (f) High-resolution cross-section HAADF-STEM image of the 2H α-In_2Se_3. (g) SEM image of the transferred α-In_2Se_3 film. (h) AFM image of the α-In_2Se_3thin layers and corresponding height profile of 15 nm. (i) OOP phase and amplitude hysteresis loop of α-In_2Se_3 on n-Si substrate via PFM.

hybrid dimensional heterojunctions, strain engineering, gate voltage, and other local field enhancement methods.[3] In recent years, the method of ferroelectric local field modulation has been applied in a variety of scientific fields, including superconductivity, excitons, photocatalysis, energy storage, and specially electronic devices.[16−20] Ferroelectric modulation provides benefits over other techniques for multipurpose photoelectric devices, namely low power consumption and selective modulation of the background carrier concentration via ferroelectric local field effects.[21−23] However, familiar ferroelectric materials (for example, PZT and PVDF) are either insulators or wide bandgap semiconductors with weak conductivity. 2D hybrid perovskites ferroelectric materials have superior photoelectric capabilities but are unstable and poisonous to heavy metals, which further limits their practical applications.[24] Fortunately, functional 2D ferroelectric materials can demonstrate considerable modulation capabilities in channel conductance, which presents significant promise for next-generation integrated optoelectronic systems.[11,25]

In recent years, α-In_2Se_3 with a noncentrosymmetric crystal structure has been discovered as a stable 2D vdW ferroelectric semiconductor.[26−28] The ferroelectric polarization of α-In_2Se_3 can also be switched by the sweeping voltage because of its out-of-plane (OOP) and in-plane (IP) polarization dipole locking.[28,29] On the other hand, α-In_2Se_3 exhibits a suitable thickness-dependent direct bandgap and excellent photoelectric performances with a strong optical absorption in visible to near-infrared wavelengths, making α-In_2Se_3 a potential candidate for photodetection.[11] Some α-In_2Se_3-based photodetectors[30−38] have been reported, but most of these devices require a voltage to operate, and there is no synergy to enhance the optimal parameters (such as light/dark current ratio or detectivity) and the response speed. Considering the ferroelectric local field regulates and enhances heterojunction built-in electric fields, it is possible to design a photodetector that simultaneously achieves a fast response, high sensitivity, and low power consumption.[25,39] Moreover, it is worth noting that few researchers pay attention to the detailed relation between the α-In_2Se_3 ferroelectricity and the photoresponse of the device.

https://doi.org/10.1021/acsnano.2c11925
ACS Nano 2023, 17, 6534−6544

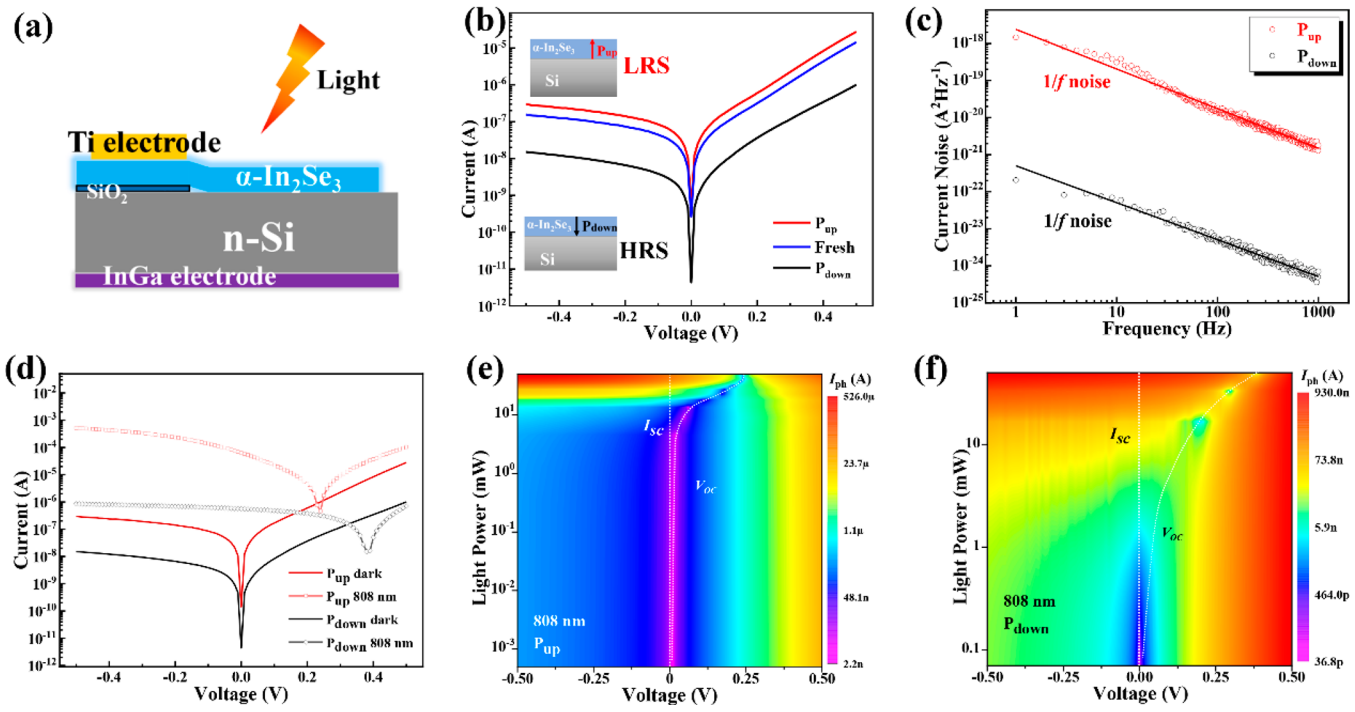

Figure 2. Electrical and photovoltaic characterizations of the α-In_2Se_3/n-Si ferroelectric heterojunction. (a) Schematic of the hybrid dimensional heterojunction. (b) *I*–*V* curves of the heterojunction with three states. (c) Comparison of the noise current spectral density. (d) *I*–*V* characteristics of photovoltaic behaviors with $P_{up/down}$ states under 808 nm illumination with 50 mW. (e) and (f) Photocurrent mapping as a function of bias and light power at $P_{up/down}$ states, respectively. Open-circuit voltage and short-circuit current are indicated by dotted lines.

In this work, we report an efficient optoelectronic device based on an α-In_2Se_3/Si junction with an easy-to-prepare vdW vertical heterostructure. The device exhibits robust multilevel conduction switching modulated by ferroelectric polarization and photoexcitation. In view of the simultaneous effects of the ferroelectric polarization field and the electric field built into the heterojunction, the photodetector in the ferroelectric polarization up state attains a self-powered, highly sensitive photoresponse as well as shows a rapid frequency response. Surprisingly, the photoresponse determined by incident light power and wavelength can be modulated by tuning different ferroelectric remanent polarization states. A competitive relationship was found between the enhancement photoresponsivity ratio via ferroelectric modulation and the photovoltaic effect of the photodiode. In addition, high-resolution NIR imaging was demonstrated in the photodetector with different polarization states, indicating the reliability and tunability of our device. This work highlights the potential of the great modulation capabilities and the enhancement of optoelectronic performance based on ferroelectric semiconductor vdW heterojunction photodetectors.

2. RESULTS AND DISCUSSION

Figure 1a shows the schematic atomic structure of layered α-In_2Se_3 which contains five covalently bonded atomic layers in the order of Se−In−Se−In−Se. The spatial symmetry breaks of the asymmetry lead to electric dipoles at different directions, resulting in ferroelectric properties in α-In_2Se_3 in out-of-plane (OOP) and in-plane (IP) directions.[26,40] The synthesized 2D layered In_2Se_3 by the atmospheric pressure chemical vapor deposition (APCVD) method is introduced in Experimental Methods. A schematic of the growth and growth-time-dependent optical images of α-In_2Se_3 films is shown in Figure S8. Raman spectroscopy is performed in the as-grown α-In_2Se_3 on fluorophlogopite mica (F-mica) with the corresponding Raman spectra with 532 nm laser excitation shown in Figure 1b. Quadruple prominent characteristic peaks (E_g mode at 89 cm^{-1} and A(LO+TO), A(TO), A(LO) phonon mode at 104, 181, 203 cm^{-1}) can be observed, which are similar to reported 2H α-In_2Se_3 results.[27,29,41,42] XRD patterns of the transferred α-In_2Se_3 film on the Si substrate have been synthesized using X-ray diffraction. All clear diffraction peaks in Figure1c, where the strongest diffraction peak (004) is located at 18.6°, are consistent with the data of the In_2Se_3 (JCPDS 34-1279). The XRD pattern of the synthesized α-In_2Se_3 film along the same F-mica crystal plane (001) ordination by a van der Waals epitaxial mode is shown in Figure S2. The crystal structure of the ferroelectric α-In_2Se_3 films belongs to the hexagonal structure and *P*63/*mmc* symmetry, according to the reconfirmed Raman and XRD characteristics. Furthermore, the high quality synthesized 2H α-In_2Se_3 is unambiguously confirmed by aberration-corrected scanning transmission electron microscopy (STEM).[43] The cross-sectional atomic-scale high angle annular dark field (HAADF) image (Figure 1c) clearly shows the 2H α-In_2Se_3 stacking structure.[43,44] The chemical states of In $3d_{3/2}$ and $3d_{5/2}$ can be proven from the peaks in the binding energy of 452.2 and 444.5 eV (Figure 1d, left); meanwhile the peaks at 54.45 and 53.58 eV (Figure 1d, right) are related to the $3d_{3/2}$ and $3d_{5/2}$ states of Se, respectively.[45] From X-ray photoelectron spectroscopy (XPS) results, the film consists of In and Se atoms showing an In:Se stoichiometry atomic ratio of 2:3 in Figure S3. Ultraviolet−visible-near-infrared absorption spectroscopy was investigated (Figure 1e) about the α-In_2Se_3 film on a transparent F-mica substrate (see Figure S9 of the optical image of the films sample). By using the Tauc Plot method, the α-In_2Se_3 film has an optical bandgap of 1.46 eV as a direct bandgap material. The

https://doi.org/10.1021/acsnano.2c11925
ACS Nano 2023, 17, 6534−6544

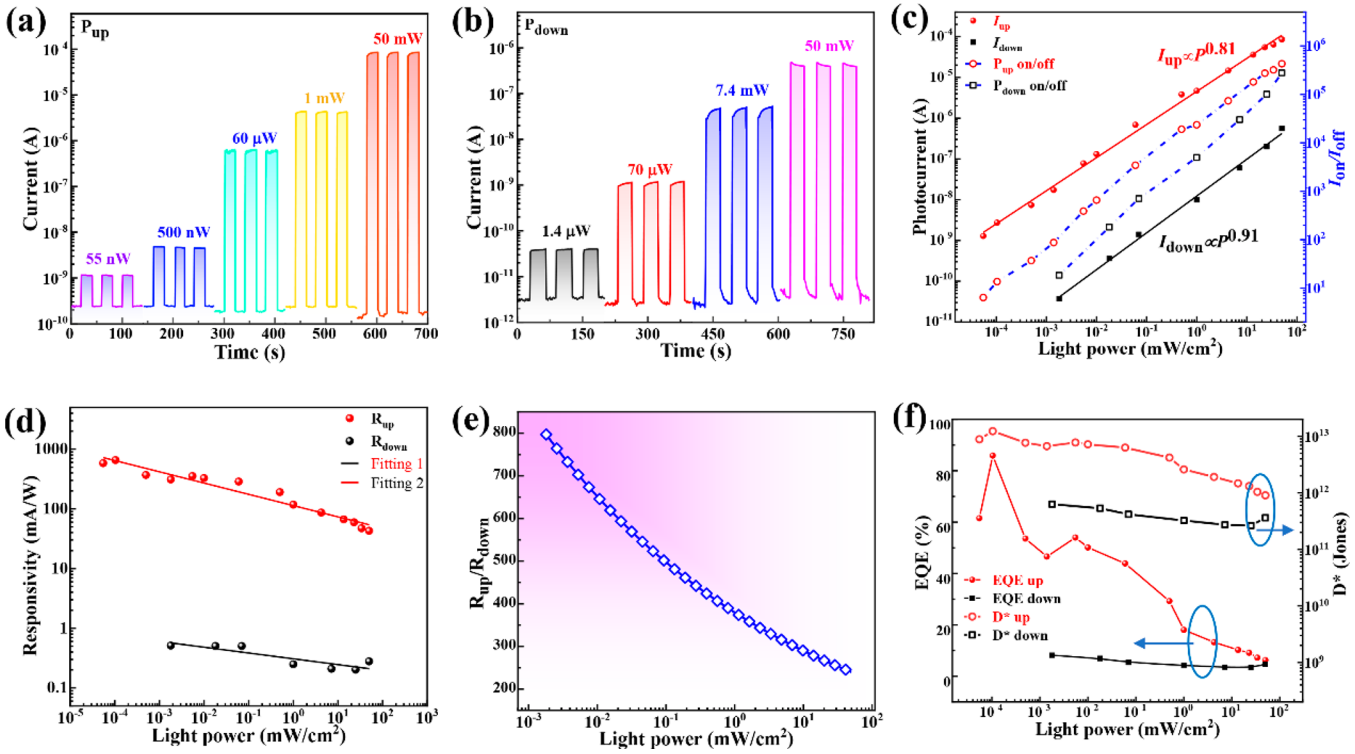

Figure 3. High performance of the self-powered ferroelectric photodetector. (a) and (b) Time-resolved photoresponse at the $P_{up/down}$ state (808 nm, V_{bias} = 0 V), respectively. (c) Photocurrent and current on/off ratio. (d) Responsivity and fitting curves. (e) The responsivity ratio between the two polarization states. (f) EQE and detectivity as a function of light power.

aforementioned findings indicate that a 2D 2H α-In_2Se_3 film of excellent quality has been achieved.

A α-In_2Se_3/n-Si heterojunction is prepared by the solution transfer method (see Experimental Methods). Figure 1e shows an SEM image of the continuous and uniform α-In_2Se_3 film on n-Si substrate. And the Raman spectrum (Figure S5) after the transferred α-In_2Se_3 to n-Si substrate is without an obvious peak shift compared in Figure 1b, indicating the success of transferring the α-In_2Se_3 film. As presented in Figure 1h, the thickness of the In_2Se_3 characterized atomic force microscopy (AFM) is confirmed to be 15 nm with nearly 15 layers, and the height of the monolayer is 1 nm from Figure S4. PFM measurements were performed to study the out-of-plane ferroelectric hysteresis behavior of α-In_2Se_3/n-Si. The local electric polarization switching measurements were carried out by varying the bias to the α-In_2Se_3 film on the heavily doped Si substrate with the conductive Pt/Ir tip. A typical localized OOP phase hysteretic loop and butterfly amplitude loop are shown in Figure 1i, and the 180° rotating phase switches depict the ferroelectricity of the produced α-In_2Se_3 film. The obtained coercive voltages are around +1.8 and −1.2 V from Figure 1i. The OOP PFM phase image of different ferroelectric domains (Figure S7a) shows distinct ferroelectric domains, where a phase contrast of 180° is observed between the neighboring domains at the red line (Figure S7b). The OOP phase and amplitude images (Figure S7c,d) of domain engineering acquired after writing two square patterns with opposite tip voltages (−10 and +10 V) demonstrate that the polarization direction can be controlled by the external voltage.[40]

In order to systematically study the modulation of electronic and photoelectric properties by this ferroelectric polarization field, a device based on the hybrid-dimension α-In_2Se_3/Si vertical heterojunction was designed. A schematic of the device is depicted in Figure 2a, and the optical image of the device is shown in Figure S9. First, the reconfigurable electronic properties of the device are characterized. Figure 2b shows the logarithmic I−V curves of the device under darkness at room temperature with the α-In_2Se_3 different states of fresh, polarized up and down, where polarization states are generated by a voltage pulse mode to highlight the role of nonvolatile ferroelectric polarization. Obviously, the ferroelectric polarization states have considerable impacts on conductivity of the junction. For a ferroelectric memory device, it is usable for a high current ratio of at least 200 from the low resistance state (LRS) of P_{up} to the high resistance state (HRS) of P_{down}.[46] Moreover, there clearly is a rectification effect in the heterojunction I−V characteristics (see Figure 2b and Figure S10c), while the individual α-In_2Se_3 and n-Si are not observed in Figure S10a,b and Figure S11 within ±0.5 V. The spectra of current noise power density in the dark were measured in Figure 2c, where a $1/f$ noise behavior dominates in the low-frequency region. Weak generation-recombination noise produced in the heterojunction may be the cause of the low noise current (10^{-18} A^2/Hz for P_{up} state and 2×10^{-22} A^2/Hz for P_{down} state) and dark current (0.3 nA at P_{up} state and 4 pA at P_{down} state), which are advantageous for enhancing the ability to detect weak light signals.[47] The modulation of the noise current by the ferroelectric polarization state is agreement with the I−V characteristics.

The photoresponse properties of the α-In_2Se_3/n-Si heterojunction under P_{up} and P_{down} states were mainly investigated. Figure 2d shows the I−V curves of the photodetector under dark and 808 nm illuminated conditions, which exhibit obvious photovoltaic characteristics. The device obviously shows stable multistage conductivity under the regulation of illumination and ferroelectric polarization, indicating potential applications in optoelectronic memory devices and logic circuits.[48,49] As a

https://doi.org/10.1021/acsnano.2c11925
ACS Nano 2023, 17, 6534−6544

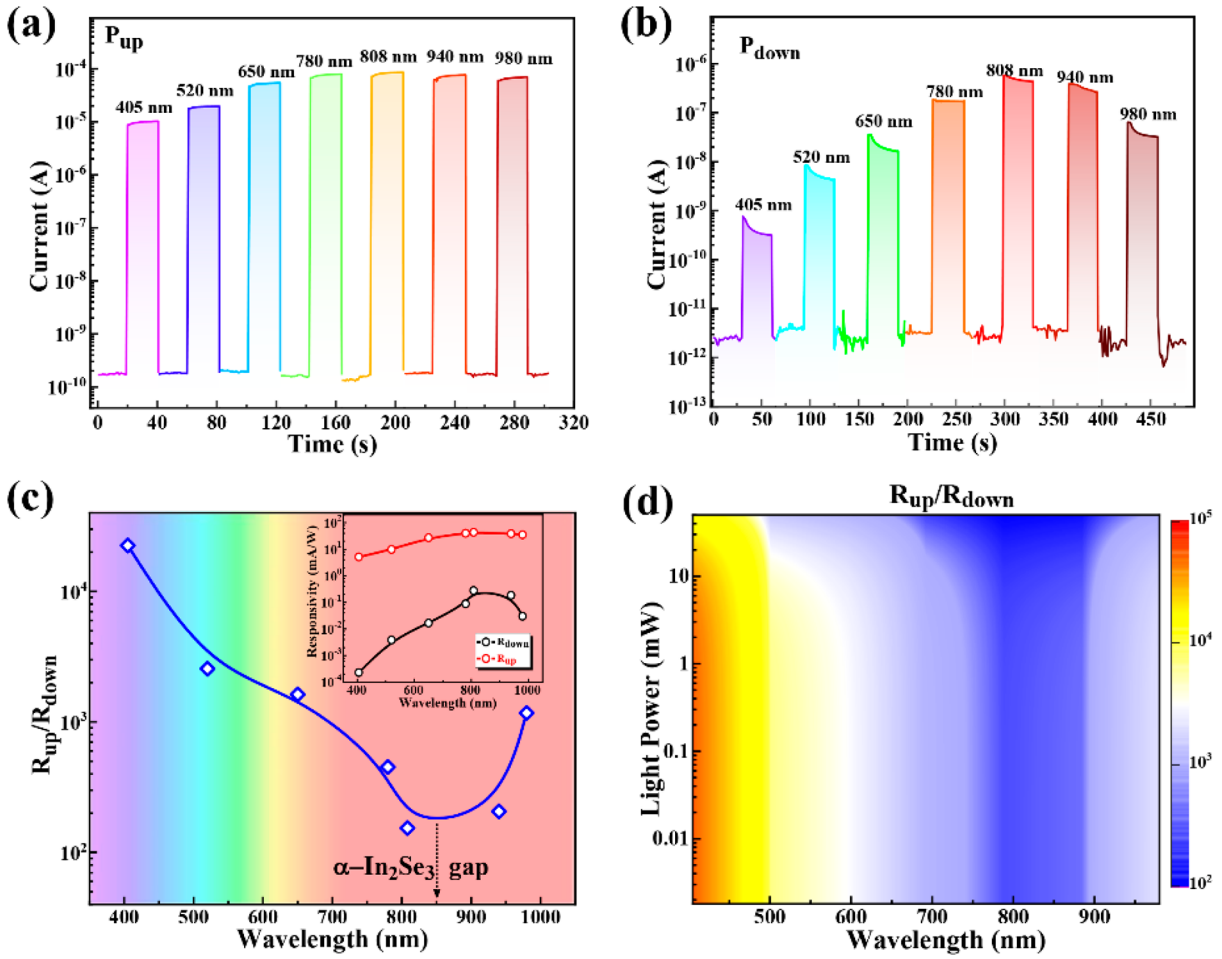

Figure 4. Ferroelectric enhancement and modulation of broadband photodetection. (a) and (b) Time-resolved photoresponse of the photodetector at the P_{up} and P_{down} state under the different incident wavelengths, respectively (uniform light power ~50 mW, V_{bias} = 0 V). (c) The responsivity ratio of the two polarization states as a function of incident light wavelength. The inset shows the responsivity under these illuminations at two polarized states. (d) The huge modulated photoresponsivity ratio simulated distribution as a function of incident wavelength and power.

critical characteristic, the illumination intensity-dependent photoresponse properties of the α-In_2Se_3/n-Si heterojunction was investigated for evaluating photodetectors. As shown in Figure 2e,f, the logarithmic current mapping characteristics under two polarized states as a function of bias voltage with 808 nm illumination power. The $I-V$ curves in a broader light power range are exhibited in Figure S12a,b. Because of the increased number of photocarriers produced by the photovoltaic effect mode, both the short-circuit current (I_{SC}) and open-circuit voltage (V_{OC}) increase collaboratively with the light power. The maximum V_{OC} is approximately ~240 mV with the P_{up} state and ~400 mV with the P_{down} state, respectively.

The time-resolved photoresponse switching behaviors with the increasing incident power in the corresponding polarization state are depicted in Figure 3a,d at zero bias. The self-powered photodetector is highly sensitive to the incident light and can be reversibly and stably switched between high- and low-conductance states, showing a maximal I_{on}/I_{off} ratio of ~4.5 × 10^5 of P_{up} state and 3 × 10^5 of the P_{down} state under illumination of 808 nm laser of 50 mW. The power-law relationship (eq 1) between the photocurrent and the laser power is expressed as

$$I_{ph} = BP^{\theta} \tag{1}$$

where I_{ph} denotes the photocurrent, B is a constant, P is the optical power, and θ is a fitting parameter representing the degree of linearity of the photodetector. Here, θ is evaluated as 0.81 and 0.91 (better linearity performance) under the P_{up} and P_{down} state, respectively (see Figure 3c). A nearly ideal power exponent (ideal θ = 1) of 0.91 describes a lower recombination of photogenerated carriers in the α-In_2Se_3/n-Si heterojunction.[50,51] Responsivity (R), the external quantum efficiency (EQE), and specific detectivity (D^*) are vital parameters of quantitatively evaluating the performance of photodetectors. R is defined as the photocurrent generated per unit power of light incident on the active area (eq 2), EQE is the ratio between the number of photoexcited electron−hole pairs contributing to the photocurrent and the number of incident photons (eq 3), while D^* reflects the ability of a photodetector to detect weak light signals (eq 4). These three parameters can be calculated from the formula

$$R = \frac{I_{ph}}{P \times S} \tag{2}$$

$$\mathrm{EQE} = R \times \frac{hc}{e\lambda} \tag{3}$$

https://doi.org/10.1021/acsnano.2c11925
ACS Nano 2023, 17, 6534−6544

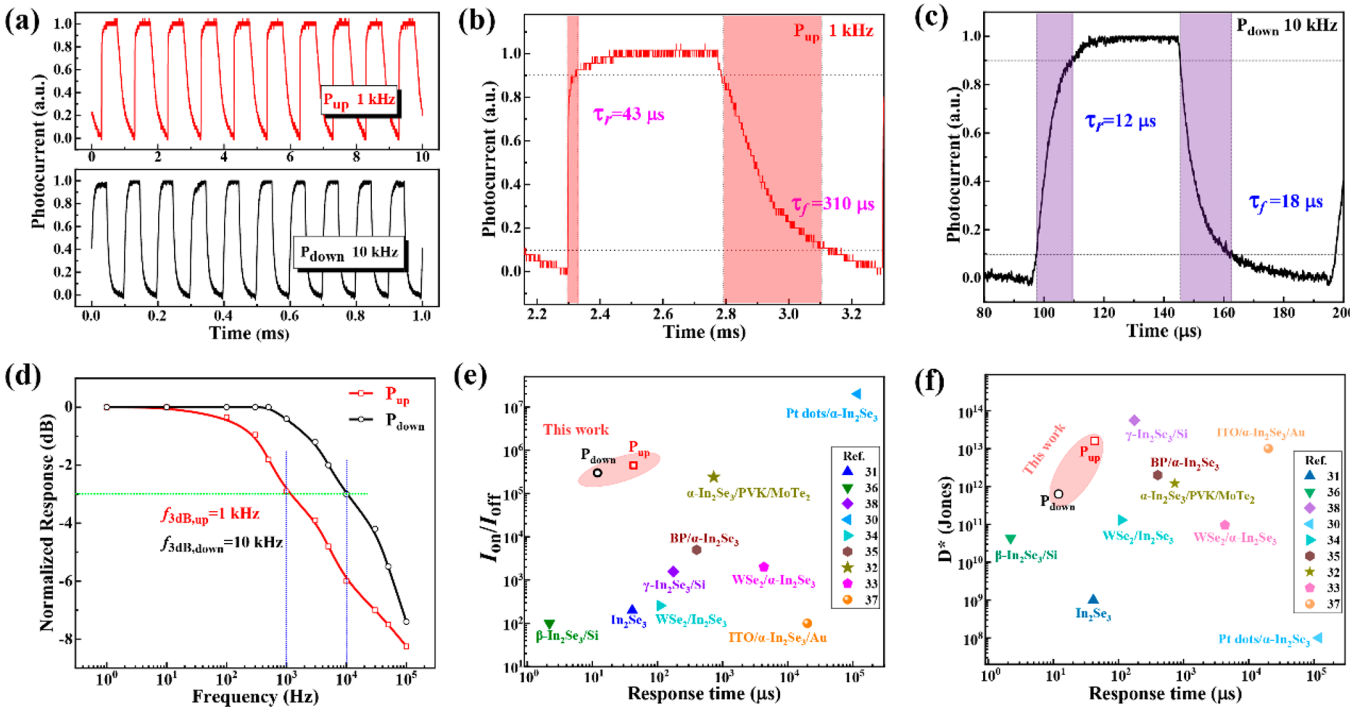

Figure 5. Response time of the α-In_2Se_3/n-Si heterojunction photodetector. (a) Time-resolved photoresponse at zero bias under an 808 nm laser of 1 and 10 kHz pulse illumination at the $P_{up/down}$ state. (b) and (c) Photoresponse time of the photodetector at the P_{up} and P_{down} state, respectively. (d) Normalized photoresponse as a function of frequency. (e) and (f) Comparison of the current on/off ratio and detectivity of the reported In_2Se_3-based photodetectors. References of information support above the two charts can be found in Table 1.

$$D^* = \frac{R \times A^{1/2}}{(2eI_{dark})^{1/2}} \quad (4)$$

where P represents input light power, S represents the effective channel excitation area, and A is the effective area of the device. Figure 3d shows the power-dependent responsivity of the photodetector of two polarized states at zero bias. The photodetector of the P_{up} state achieves maximum level photoresponsivity up to 560 mA/W under illumination of 808 nm laser with 55 nW. It is obvious that the responsivity of the photodetector in different ferroelectric polarization states have excellent differences. We define the enhancement photoresponsivity factor to be equal to the ratio of the responsivity of the P_{up} to P_{down} state (namely the R_{up}/R_{down} ratio). The light power-dependent enhancement photoresponsivity ratio is plotted in Figure 3e, and the ratio increases as the light power decreases. Figure 3f shows the EQE and D^* as a function of the laser power at 808 nm wavelength and 0 V. The photodetector of the P_{up} state achieves maximum EQE and D^* values of 83% and 1.6×10^{13} Jones, respectively. The value of assessment of R, EQE, and D^* will reduce when increasing the light power, due to the enhanced recombination activity of photoexcited electrons and holes at a higher light power.

The time-resolved photoresponse of the photodetector under different wavelength continuous-laser illuminations at zero bias is shown in Figure 4a,b with the P_{up} and P_{down} state, respectively. NIR (980, 940, 808, and 780 nm) and visible (650, 520, and 405 nm) lasers are used for light sources, which their illumination power densities are set to 50 mW/cm^2 for uniform accurate comparison. Obviously, the α-In_2Se_3/Si heterojunction exhibits an excellent photoresponse and impressive I_{on}/I_{off} ratio (over 10^5) in the broad spectral region of 405−980 nm. It is observed in Figure 4b that there is the obvious pyroelectric photocurrent contributed by the pyroelectric effect. The discussion and conjecture about this point is detailed in Figure S13. Nevertheless, there apparently is the difference of photoresponse to different wavelengths between the P_{up} and P_{down} state. The responsivity and enhancement photoresponsivity ratio (R_{up}/R_{down}) with wavelength-dependence were calculated in the inset and Figure 4c, respectively. Fitting a curve to the enhancement photoresponsivity factor with distinct inflection points, it can be concluded that the minimum ratio is almost located in the wavelength (800−900 nm) of the α-In_2Se_3 optical bandgap. When the incident light wavelength is farther from the special band, the R_{up}/R_{down} ratio modulated by α-In_2Se_3 ferroelectric polarization is going to increase. The modulation based on ferroelectric polarization of α-In_2Se_3 competes probably with the photoresponse properties. In other words, if the incident photons energy of the heterojunction is closer to the bandgap of α-In_2Se_3, the photovoltaic behavior of the photodiode should dominate.

In view of two freedom degrees of the incident light about the wavelength and the light power, the distribution trend of the enhancement photoresponsivity ratio is plotted in Figure 4d. At the incident wavelength of 405−980 nm and light power of 0.01−50 mW, the calculated enhancement photoresponsivity ratio of ferroelectric modulation is from 10^2 to 10^5. On the one hand, as the incident light power decreases, the responsivity ratio increases; on the other hand, when the incident light wavelength keeps away from the α-In_2Se_3 optical bandgap, this modulation phenomenon will be enhanced. While the wavelength of the incident light is closer to the bandgap and the incident light power is larger, the photovoltaic behavior of the photodetector must be dominantly stronger. Thus, the negative correlation relation can be revealed between the enhancement photo-

https://doi.org/10.1021/acsnano.2c11925
ACS Nano 2023, 17, 6534−6544

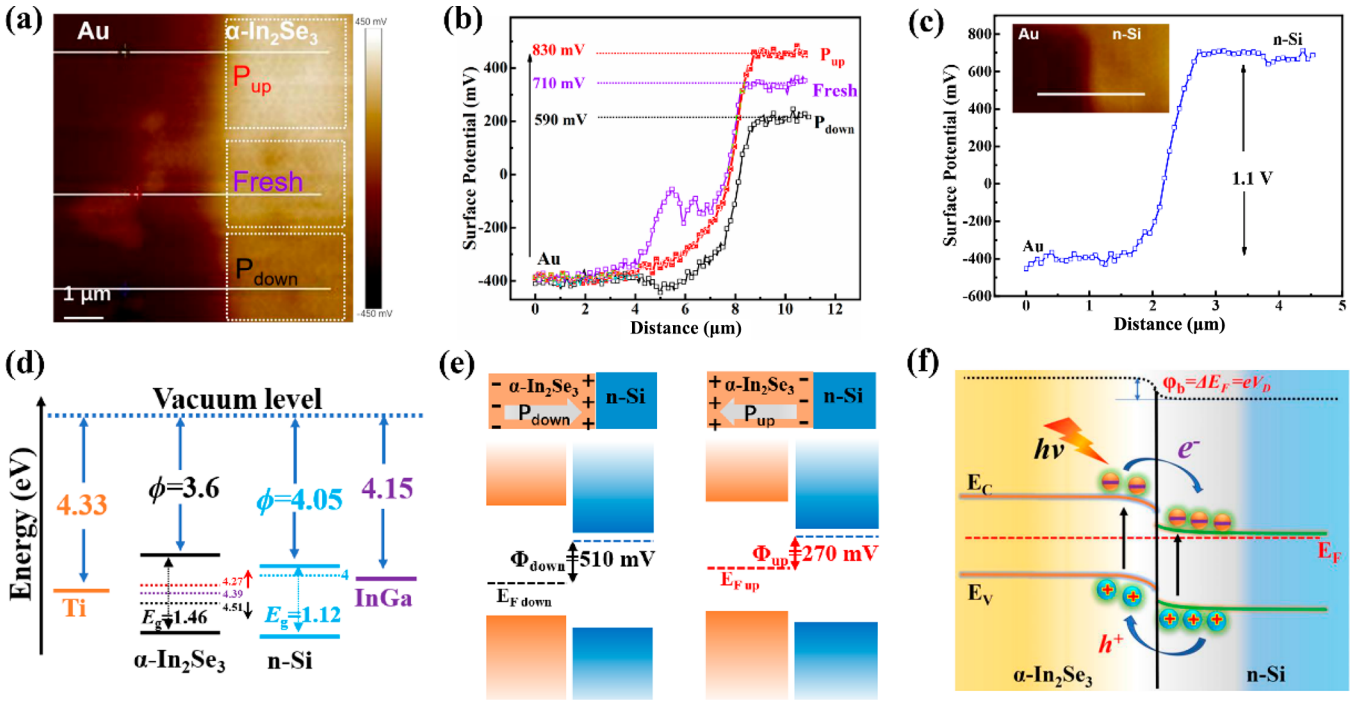

Figure 6. Working mechanism of the α-In_2Se_3/n-Si heterojunction. (a) KPFM image of Au and α-In_2Se_3 flakes. (b) Surface potential between Au and the α-In_2Se_3 in three polarized states after poling via AFM conductive tip bias (±10 and 0 V). Surface potential profiles along with the corresponding cuts lines in (a). (c) Surface potential between Au and n-Si. Inset: KPFM image of Au and n-Si. (d) Energy band alignments for the Ti, α-In_2Se_3, InGa, and n-Si before contact. (e) Energy band alignments of the α-In_2Se_3/n-Si junction before two polarized recontact. (f) Energy band alignments when the junction works under illumination without bias.

responsivity ratio by ferroelectric modulation and the photovoltaic effect of the photodiode.

The α-In_2Se_3/Si heterojunction shows not only self-powered broadband and high-sensitivity photodetection capabilities, but also a fast response to rapidly switching optical signals. The dynamic time-resolved photoresponse (Figure 5a) was investigated at the P_{up} and P_{down} states to examine the impact of ferroelectric modulation on the photoresponse time. The time intervals when the photocurrent transforms from 10% to 90% of the peak value are defined by the rise/fall times. The rise (τ_r) and fall (τ_f) times from these fast dynamic responses are approximately calculated as 43−310 μs at the P_{up} state and 12−18 μs at the P_{down} state, respectively, as shown in Figure 5b,c. Furthermore, the normalized photoresponse of our photodetector as a function of the modulated frequency is shown in the Figure 5d. The cutoff frequencies ($f_{3\ dB}$) with the photoelectrical bandwidth at two polarization states are estimated to be 1 kHz and 10 kHz, respectively. These sensitive dynamic photoresponse are superior to the reported In_2Se_3-based photodetectors. Figure 5e,f depicts the comparison of the I_{on}/I_{off} ratio and detectivity comparison with responses times about other 2D In_2Se_3-based photodetectors at room temperature.[30−38] The α-In_2Se_3/n-Si heterojunction photodetector (in red) exhibits an ultrahigh light I_{on}/I_{off} ratio and detectivity under maintaining rapid response. Moreover, the photodetector can maintain an initial photoresponse within 5000 photoresponse cycles (Figure S14a) and keep the photocurrent at least 93% after 6 months (Figure S14b), displaying the robust reproducibility and stability of our device.

To clarify the physical mechanism of the ferroelectric modulated α-In_2Se_3/Si heterojunction, all interface contact barriers were investigated. First, the band gap (~1.5 eV) of 15 layers of α-In_2Se_3 film was calculated. The result is shown in Figure S1, which is comparable to the value obtained by the absorption spectrum (Figure 1e). Further, the top surface potential of α-In_2Se_3 regions with three polarization states was characterized by using Au substrate to calibrate the work function of AFM tip used in the Kelvin probe force microscopy (KPFM) test. The surface potential difference of antiparallel OOP polarized domains with Au (Au work function = 5.1 eV) is shown in Figure 6a,b, which indicates the Fermi level (E_F) of the α-In_2Se_3 modulated by the ferroelectric local electric field. The phenomenon is similar to that reported by Tang et al.[52] Meantime, the surface potential between Au and n-Si was measured as shown in Figure 6c. Next, the working function of the In_2Se_3 flake and n-Si were calculated according to the surface potential difference of Figure 6b,c. Figure 6d illustrates the positions of the E_F relative to the energy bands of α-In_2Se_3 and n-Si before contacts, which indicates favorable Ohmic contact.[53,54] Thus, the E_F of the α-In_2Se_3 P_{up} state is higher than that of the P_{down} state in the heterojunction interface. When the α-In_2Se_3 constructs a heterojunction with n-Si, the charge distribution will be reconstructed to ensure the dynamic balance of diffusion carriers at the interface of this junction until the Fermi levels are aligned. The electric field of the junction interface can be enhanced or inhibited by the α-In_2Se_3 ferroelectric field, leading to the accumulation or depletion of carriers.[55] It also means that the barrier height (Φ) across the junction and electromotive force (EMF) with illumination can be modulated by the ferroelectric remanent polarization field after reconstruction as illustrated in Figure 6e.[11] Consequently, the energy levels near the Si surface bent upward, and the energy levels near the α-In_2Se_3 surface are bent downward, leading to the formation of a built-in electric field at the α-In_2Se_3/n-Si interface. The electrons and holes are then rapidly separated by the built-in electric field and collected by the respective electrodes, ultimately generating

https://doi.org/10.1021/acsnano.2c11925
ACS Nano 2023, 17, 6534−6544

Table 1. Comparison of Device Performance Parameters of In_2Se_3-Based Photodetectors

device	self-powered	λ (nm)	I_{on}/I_{off}	R (mA/W)	D^* (Jones)	response time (μs)	ref
In_2Se_3 film	30 V	405−730	200	1	_	41	31
β-In_2Se_3/Si	−2 V	265−1300	100	6400	4.3×10^{10}	2.2	36
γ-In_2Se_3/Si	−1 V	380−880	1570	5670	5.6×10^{13}	175	38
Pt nanodots/α-In_2Se_3	3 V	visible	2×10^7	_	_	118 ms	30
WSe_2/In_2Se_3	−1 V	405−905	256	1840	1.3×10^{11}	110	34
BP/α-In_2Se_3	20 V	473−1550	5000	1000	2×10^{12}	400	35
α-In_2Se_3/PVK/$MoTe_2$	yes	473−639	2.4×10^5	287.6	1.2×10^{12}	730	32
WSe_2/α-In_2Se_3	−3 V	520−980	2000	2210	9.5×10^{10}	4.3 ms	33
ITO/α-In_2Se_3/Au	yes	520−780	100	1000	10^{13}	20 ms	37
α-In_2Se_3/Si (P_{up})	**yes**	**405−980**	**4.5×10^5**	**560**	**1.6×10^{13}**	**43**	**this work**
α-In_2Se_3/Si (P_{down})	**yes**	**405−980**	**3×10^5**	**26.6**	**6.3×10^{11}**	**12**	

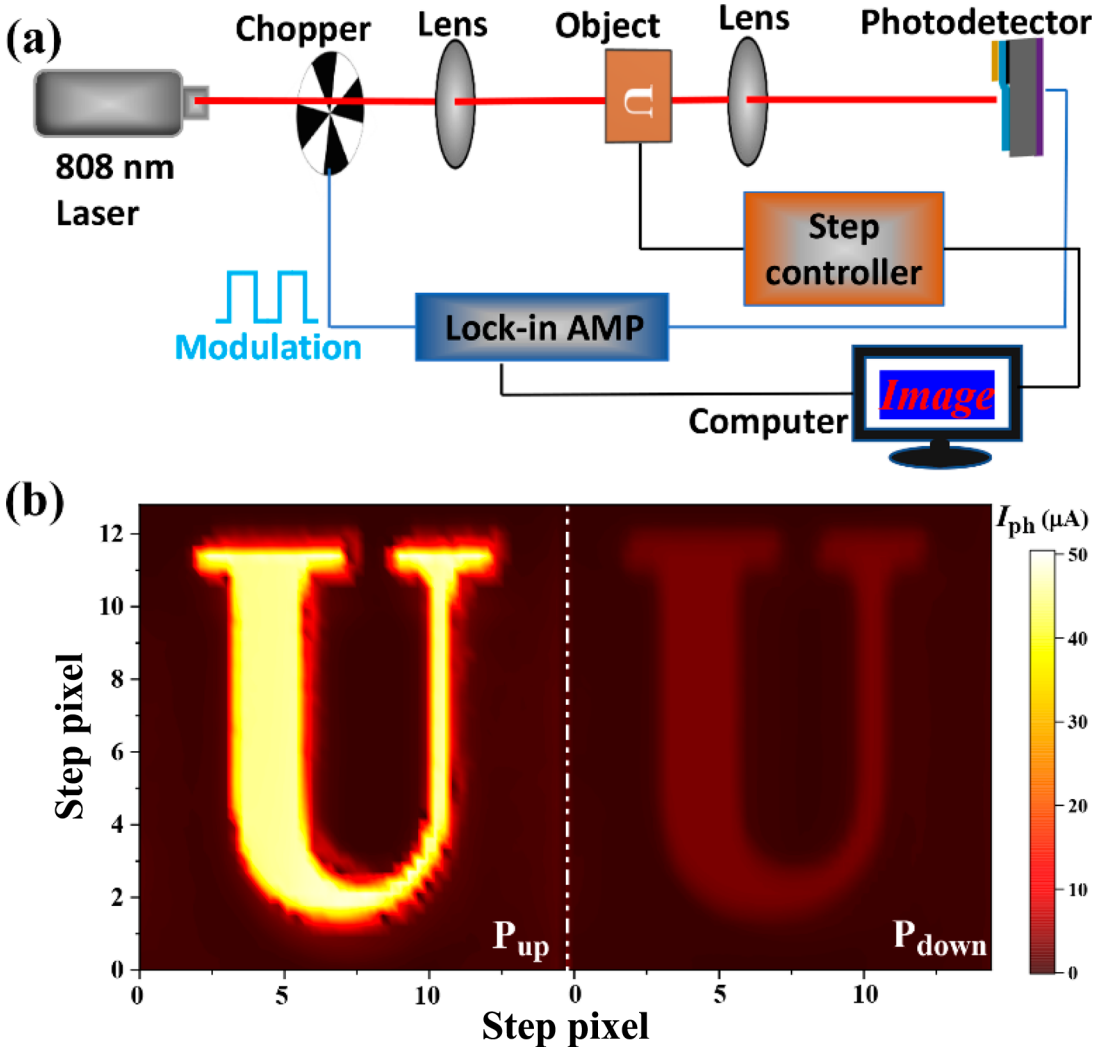

Figure 7. NIR imaging application. (a) Schematic of the instrumentation system for imaging application. (b) The imaging results of the "U" pattern under 808 nm illumination with P_{up} and P_{down} states, respectively.

the photocurrent (Figure 6f). Deservedly, the built-in field at the junction interface can realize self-powered fast optical detection through the photovoltaic effect. As a matter of course, the internal potential barrier height (Φ_{up} = 270 mV< Φ_{down} = 510 mV) impacts electrical and photoelectrical transportation properties of the heterojunction. Therefore, the ferroelectric remanent electric field in the same direction as the built-in field can significantly enhance the current in the P_{up} state; on the contrary, the conduction will be inhibited in the P_{down} state.

On the basis of the excellent optoelectronic performance of the device under light irradiation, we conducted a single-pixel imaging experiment.[56] Figure 7a displays the setup of the single-pixel imaging technique. A metal mask with a hollow English letter "U" controlled by a 2D motorized stage was put between the 808 nm laser and the device. With the movement of the mask, the position-dependent current of the device could be recorded in real time by a lock-in amplifier, which was further transformed into a current mapping image. Figure 7b shows the

https://doi.org/10.1021/acsnano.2c11925
ACS Nano 2023, 17, 6534−6544

infrared clear and high-resolution images measured in the two polarization states, demonstrating the repeatability and stability of our device. The imaging in two polarization states shows that the strong contrast of photocurrent can represent the 1 and 0 states. Importantly, owing to the outstanding photosensing (incident light wavelength and power) and the robust ferroelectric switch of our photodetector, the signal readout of image response can be individually tunable. The "on" and "off" state of the device can be ensured only by modulating the ferroelectric polarization state with a bias pulse while maintaining the illumination, which implies potential applications in optoelectronic logic devices and photonic chips.

3. CONCLUSION

In summary, a self-powered broadband high-sensitivity α-In_2Se_3/n-Si heterojunction photodetector has been successfully prepared. The photodetector displays outstanding photodetection with low noise and dark current (0.3 nA/4 pA), a significant I_{light}/I_{dark} ratio ($4.5 \times 10^5/3 \times 10^5$) and quick photoswitching response (12/43 μs) at the P_{up}/P_{down} states, respectively. Moreover, the device exhibits a strong self-regulating ability of electrical properties and photoresponse via ferroelectrically polarized modulation. The ferroelectric polarization in α-In_2Se_3 provides a strategy for enhancement and modulation of photodetection. Under ferroelectric modulation, the responsivity could be enhanced 10^5 in the incident light range of 405−980 nm with a power of 1×10^{-3}−50 mW. This investigation of the ferroelectrically modulated photodetector illustrated the competitive relation between the photovoltaic behavior of the heterojunction and the enhancement photoresponsivity ratio of α-In_2Se_3 ferroelectric modulation. A high-resolution NIR on/off-states imaging demonstration has further confirmed the dependability and adjustability of our technology. The results will have a certain referential significance and also greatly enrich the functionalities of the ferroelectric modulated photodetector.

4. EXPERIMENTAL METHODS

Preparation Method of α-In_2Se_3 Film. The 2D α-In_2Se_3 nano films were grown on fluorphlogopite mica ($[KMg_3(AlSi_3O_{10})F_2]$) substrates (F-mica) via the APCVD method. The precursors were placed on separate quartz boats, and the superfluous Se source was placed upstream. The F-mica substrate was placed 2−5 mm above In_2O_3 powders (100 mg). The Se source and In_2O_3 powders were used as the precursors with 10/50 sccm H_2/Ar mixed gas as the carrier gas. After fully vacuuming and air-washing, the Se source and In_2O_3 powders were heated to 300 and 660 °C in 15 min, respectively, and the temperature was held for 30 min at atmospheric pressure. The large sized films were synthesized in a confined space growth CVD method and by controlling the gas flow rate and growth time. Subsequently, the hydrogen is turned off and the argon gas still is maintained at 50 sccm, and the CVD tube furnace was cooled naturally down to room temperature.

Transfer of α-In_2Se_3 Film. The prepared polystyrene (PS) solutions (~1.5 g of PS tiny particles was fully dissolved in 10 mL of toluene) were spin coated onto α-In_2Se_3/F-mica. The PS/α-In_2Se_3/F-mica was heated at 90 °C for 10 min to solidify the PS films. The edges of PS/α-In_2Se_3/F-mica were scraped and then floated on the surface of deionized water. When the separated PS/α-In_2Se_3 film was transferred onto target substrates (like SiO_2 or n-Si substrate), a baking step (at 100 °C for 5 min) was carried out to remove the water residues. Finally, the transfer process was accomplished by dissolving the polystyrene on the surface with toluene and then blowing it dry with nitrogen gas.

Characterizations of α-In_2Se_3. The as-synthesized α-In_2Se_3 films were characterized by using Raman spectrometry (LabRAM HR Evolution), XRD (Rigaku SmartLab), XPS (Kratos Axis supra+), UV−vis-NIR spectrometry (Shimadzu 3700), STEM (JEM ARM-200F), SEM (Hitachi SU8220), AFM & PFM & KPFM (Bruker Dimension Icon). PFM measurements were performed with Ir/Pt conducting tips (3 N/m) with 300 kHz excitation frequency and 0.5 V drive amplitude under Dual AC Resonance-Tracking (DART) mode. Supplying the appropriate dc bias to the tip while scanning the surface with the sample surface enabled domain switching. KPFM measurements were performed with the same tips and the n-Si substrate evaporated 5 nm Ti and 100 nm Au.

Device Fabrications. The CVD-synthesized α-In_2Se_3 films were transferred onto the n-Si substrate treated with 5% hydrofluoric acid solution for the α-In_2Se_3/n-Si heterojunction device. The Ti/Au electrodes with a thickness of ~50/20 nm were deposited through a mask on the α-In_2Se_3 film via the electron beam evaporation in a vacuum ($<10^{-5}$ Pa). And an In/Ga alloy was applied evenly to the silicon substrate backside as an ohmic contact.

Electric Measurements. A Keithley 2611B and ADCMT 6242 SourceMeter were used to measure the $I-V$ and $I-t$ characteristics of the devices. The polarizing pulse voltage (±10 V) was applied through the same source/measure for the device to tune the ferroelectric polarization of α-In_2Se_3. Because OOP and IP polarization of α-In_2Se_3 are dipole-locking, the ferroelectric polarization of α-In_2Se_3 can also be switched by sweeping voltage in any direction so that pulse mode was adopted to better evaluate the above reconfigurable electronic properties. After removal of the polarization voltage, the $I-V$ and $I-t$ curves of the photoresponse were measured under different α-In_2Se_3 remanent polarization states. A function generator (Agilent 33220A) and oscilloscope (Agilent DSO-X2012A) were used to measure the response time under high photoswitching frequency. A lock-in amplifier (SR830) was used to acquire the electrical signals of the noise-current and the imaging system.

ASSOCIATED CONTENT

Supporting Information

The Supporting Information is available free of charge at https://pubs.acs.org/doi/10.1021/acsnano.2c11925.

Energy band calculations, XRD patterns, XPS spectrum, AFM topography, the synthesized α-In_2Se_3 film on F-mica; the Raman spectrum after α-In_2Se_3 film transferred to n-Si substrate; EDS mappings and EDS spectrum of the α-In_2Se_3/n-Si heterostructure; ferroelectric domain engineering of α-In_2Se_3; growth α-In_2Se_3 films; optical image of the device; $I-V$ characteristics of α-In_2Se_3/Ti, n-Si/InGa and α-In_2Se_3/n-Si; $I-V$ curves of out-of-plane α-In_2Se_3; semilogarithmic $I-V$ characteristics of α-In_2Se_3/n-Si heterojunction for photoresponse at the ferroelectric polarization state; photoresponse of photovoltaic and pyroelectric and related discussion; the stable and endurant photoresponse of the α-In_2Se_3/n-Si heterojunction photodetector. (Figures S1−S14) (PDF)

AUTHOR INFORMATION

Corresponding Authors

Cheng Jia − *Hefei National Research Center for Physical Sciences at the Microscale, University of Science and Technology of China, Hefei 230026, China; Hefei National Laboratory, University of Science and Technology of China, Hefei 230088, China;* orcid.org/0000-0002-3434-5694; Email: jiacheng20@mail.ustc.edu.cn

Yuanjun Yang − *Department of Physics, School of Physics, Hefei University of Technology, Hefei 230009, China;* orcid.org/0000-0002-6976-7416; Email: yangyuanjun@hfut.edu.cn

Hui Zhang − *Hefei National Research Center for Physical Sciences at the Microscale and Department of Physics,*

https://doi.org/10.1021/acsnano.2c11925
ACS Nano 2023, 17, 6534−6544

University of Science and Technology of China, Hefei 230026, China; Hefei National Laboratory, University of Science and Technology of China, Hefei 230088, China; Email: huiz@ustc.edu.cn

Authors

Shuangxiang Wu – *Hefei National Research Center for Physical Sciences at the Microscale, University of Science and Technology of China, Hefei 230026, China; Hefei National Laboratory, University of Science and Technology of China, Hefei 230088, China*

Jinze Fan – *Hefei National Research Center for Physical Sciences at the Microscale, University of Science and Technology of China, Hefei 230026, China; Hefei National Laboratory, University of Science and Technology of China, Hefei 230088, China*

Chaojie Luo – *Hefei National Research Center for Physical Sciences at the Microscale, University of Science and Technology of China, Hefei 230026, China; Hefei National Laboratory, University of Science and Technology of China, Hefei 230088, China*

Minghui Fan – *Hefei National Research Center for Physical Sciences at the Microscale, University of Science and Technology of China, Hefei 230026, China; Instruments Center for Physical Science, University of Science and Technology of China, Hefei, Anhui 230026, China*

Ming Li – *Instruments Center for Physical Science, University of Science and Technology of China, Hefei, Anhui 230026, China*

Lanping He – *Department of Physics, School of Physics, Hefei University of Technology, Hefei 230009, China*

Complete contact information is available at: https://pubs.acs.org/10.1021/acsnano.2c11925

Author Contributions

C.J. and H.Z. conceived the project. C.J. fabricated the devices and characterized the materials with the help of C.J.L., M.L., M.H.F., L.P.H.; C.J. and J.Z.F. carried out the electrical and optoelectronic measurements. S.X.W. calculated the electronics band structure. C.J., H.Z., and Y.J.Y. analyzed the data and wrote the manuscript with input from all authors. All authors reviewed the manuscript.

Notes

The authors declare no competing financial interest.

ACKNOWLEDGMENTS

This research was also supported by The National Natural Science Foundation of China (Grants No. 12074357, 11804324, 52072102), The Innovation Program For Quantum Science and Technology (No. 2021ZD0302800), The Chinese Academy of Sciences Pioneer Hundred Talents Program, The Open Foundation of the University of Science and Technology of China (No. KF2020002), and The Fundamental Research Funds for the Central Universities (No. wk2310000104).

REFERENCES

(1) Liu, C.; Guo, J.; Yu, L.; Li, J.; Zhang, M.; Li, H.; Shi, Y.; Dai, D. Silicon/2D-material photodetectors: from near-infrared to mid-infrared. *Light Sci. Appl.* **2021**, *10*, 123–144.

(2) Wu, F.; Li, Q.; Wang, P.; Xia, H.; Wang, Z.; Wang, Y.; Luo, M.; Chen, L.; Chen, F.; Miao, J.; Chen, X.; Lu, W.; Shan, C.; Pan, A.; Wu, X.; Ren, W.; Jariwala, D.; Hu, W. High efficiency and fast van der Waals hetero-photodiodes with a unilateral depletion region. *Nat. Commun.* **2019**, *10*, 4663.

(3) Wang, J.; Fang, H.; Wang, X.; Chen, X.; Lu, W.; Hu, W. Recent Progress on Localized Field Enhanced Two-dimensional Material Photodetectors from Ultraviolet-Visible to Infrared. *Small* **2017**, *13*, 1700894.

(4) Stewart, J. W.; Vella, J. H.; Li, W.; Fan, S.; Mikkelsen, M. H. Ultrafast pyroelectric photodetection with on-chip spectral filters. *Nat. Mater.* **2020**, *19*, 158–162.

(5) Lopez-Sanchez, O.; Lembke, D.; Kayci, M.; Radenovic, A.; Kis, A. Ultrasensitive photodetectors based on monolayer MoS_2. *Nat. Nanotechnol.* **2013**, *8*, 497–501.

(6) Michel, J.; Liu, J.; Kimerling, L. C. High-performance Ge-on-Si photodetectors. *Nat. Photonics* **2010**, *4*, 527–534.

(7) Fuentes-Hernandez, C.; Chou, W. F.; Khan, T. M.; Diniz, L.; Lukens, J.; Larrain, F. A.; Rodriguez-Toro, V. A.; Kippelen, B. Large-area low-noise flexible organic photodiodes for detecting faint visible light. *Science* **2020**, *370*, 698–701.

(8) Liu, J.; Xia, F.; Xiao, D.; Garcia de Abajo, F. J.; Sun, D. Semimetals for high-performance photodetection. *Nat. Mater.* **2020**, *19*, 830–837.

(9) Wu, D.; Jia, C.; Shi, F.; Zeng, L.; Lin, P.; Dong, L.; Shi, Z.; Tian, Y.; Li, X.; Jie, J. Mixed-dimensional $PdSe_2$/SiNWA heterostructure based photovoltaic detectors for self-driven, broadband photodetection, infrared imaging and humidity sensing. *J. Mater. Chem. A* **2020**, *8*, 3632–3642.

(10) Zeng, L.; Wu, D.; Jie, J.; Ren, X.; Hu, X.; Lau, S. P.; Chai, Y.; Tsang, Y. H. Van der Waals Epitaxial Growth of Mosaic-Like 2D Platinum Ditelluride Layers for Room-Temperature Mid-Infrared Photodetection up to 10.6 microm. *Adv. Mater.* **2020**, *32*, 2004412–2004423.

(11) Sun, Y.; Niu, G.; Ren, W.; Meng, X.; Zhao, J.; Luo, W.; Ye, Z. G.; Xie, Y. H. Hybrid System Combining Two-Dimensional Materials and Ferroelectrics and Its Application in Photodetection. *ACS Nano* **2021**, *15*, 10982–11013.

(12) Liu, L.; Wu, L.; Wang, A.; Liu, H.; Ma, R.; Wu, K.; Chen, J.; Zhou, Z.; Tian, Y.; Yang, H.; et al. Ferroelectric-Gated InSe Photodetectors with High On/Off Ratios and Photoresponsivity. *Nano Lett.* **2020**, *20*, 6666–6673.

(13) Wu, S.; Chen, Y.; Wang, X.; Jiao, H.; Zhao, Q.; Huang, X.; Tai, X.; Zhou, Y.; Chen, H.; Wang, X.; Huang, S.; Yan, H.; Lin, T.; Shen, H.; Hu, W.; Meng, X.; Chu, J.; Wang, J. Ultra-sensitive polarization-resolved black phosphorus homojunction photodetector defined by ferroelectric domains. *Nat. Commun.* **2022**, *13*, 3198.

(14) Wang, J.; Ma, J.; Yang, Y.; Chen, M.; Zhang, J.; Ma, J.; Nan, C.-W. Ferroelectric Photodetector with High Current on–off Ratio ($\sim 1 \times 10^4$%) in Self-Assembled Topological Nanoislands. *ACS Appl. Electron. Mater.* **2019**, *1*, 862–868.

(15) Lemme, M. C.; Akinwande, D.; Huyghebaert, C.; Stampfer, C. 2D materials for future heterogeneous electronics. *Nat. Commun.* **2022**, *13*, 1392.

(16) Crassous, A.; Bernard, R.; Fusil, S.; Bouzehouane, K.; Le Bourdais, D.; Enouz-Vedrenne, S.; Briatico, J.; Bibes, M.; Barthelemy, A.; Villegas, J. E. Nanoscale electrostatic manipulation of magnetic flux quanta in ferroelectric/superconductor $BiFeO_3/YBa_2Cu_3O_{(7-\delta)}$ heterostructures. *Phys. Rev. Lett.* **2011**, *107*, 247002.

(17) Zhu, H.; Liu, M.; Zhang, Y.; Yu, Z.; Ouyang, J.; Pan, W. Increasing energy storage capabilities of space-charge dominated ferroelectric thin films using interlayer coupling. *Acta Mater.* **2017**, *122*, 252–258.

(18) Wen, B.; Zhu, Y.; Yudistira, D.; Boes, A.; Zhang, L.; Yidirim, T.; Liu, B.; Yan, H.; Sun, X.; Zhou, Y.; et al. Ferroelectric-Driven Exciton and Trion Modulation in Monolayer Molybdenum and Tungsten Diselenides. *ACS Nano* **2019**, *13*, 5335–5343.

(19) Wen, Z.; Wu, D. Ferroelectric Tunnel Junctions: Modulations on the Potential Barrier. *Adv. Mater.* **2019**, *32*, 1904123.

(20) Zhang, Z.; Zou, C.; Yang, S.; Yang, Z.; Yang, Y. Ferroelectric polarization effect promoting the bulk charge separation for enhance the efficiency of photocatalytic degradation. *Chem. Eng. J.* **2021**, *410*, 128430.

(21) Zhao, X.; Song, K.; Huang, H.; Han, W.; Yang, Y. Ferroelectric Materials for Solar Energy Scavenging and Photodetectors. *Adv. Opt. Mater.* **2022**, *10*, 2101741.
(22) Liu, Y.; Ji, Y.; Xia, Y.; Wu, L.; Bowen, C. R.; Yang, Y. Enhanced photocurrent in ferroelectric $Bi_{0.5}Na_{0.5}TiO_3$ materials via ferro-pyro-phototronic effect. *Nano Energy* **2022**, *98*, 107312.
(23) Li, Q.; Wang, T.; Fang, Y.; Hu, X.; Tang, C.; Wu, X.; Zhu, H.; Ji, L.; Sun, Q. Q.; Zhang, D. W.; et al. Ultralow Power Wearable Organic Ferroelectric Device for Optoelectronic Neuromorphic Computing. *Nano Lett.* **2022**, *22*, 6435−6443.
(24) Li, L.; Liu, X.; Li, Y.; Xu, Z.; Wu, Z.; Han, S.; Tao, K.; Hong, M.; Luo, J.; Sun, Z. Two-Dimensional Hybrid Perovskite-Type Ferroelectric for Highly Polarization-Sensitive Shortwave Photodetection. *J. Am. Chem. Soc.* **2019**, *141*, 2623−2629.
(25) Jiang, Y.; Zhang, L.; Wang, R.; Li, H.; Li, L.; Zhang, S.; Li, X.; Su, J.; Song, X.; Xia, C. Asymmetric Ferroelectric-Gated Two-Dimensional Transistor Integrating Self-Rectifying Photoelectric Memory and Artificial Synapse. *ACS Nano* **2022**, *16*, 11218−11226.
(26) Ding, W.; Zhu, J.; Wang, Z.; Gao, Y.; Xiao, D.; Gu, Y.; Zhang, Z.; Zhu, W. Prediction of intrinsic two-dimensional ferroelectrics in In_2Se_3 and other III_2-VI_3 van der Waals materials. *Nat. Commun.* **2017**, *8*, 14956.
(27) Cui, C.; Hu, W. J.; Yan, X.; Addiego, C.; Gao, W.; Wang, Y.; Wang, Z.; Li, L.; Cheng, Y.; Li, P.; et al. Intercorrelated In-Plane and Out-of-Plane Ferroelectricity in Ultrathin Two-Dimensional Layered Semiconductor In_2Se_3. *Nano Lett.* **2018**, *18*, 1253−1258.
(28) Li, Y.; Chen, C.; Li, W.; Mao, X.; Liu, H.; Xiang, J.; Nie, A.; Liu, Z.; Zhu, W.; Zeng, H. Orthogonal Electric Control of the Out-Of-Plane Field-Effect in 2D Ferroelectric α-In_2Se_3. *Adv. Electron. Mater.* **2020**, *6*, 2000061.
(29) Xiao, J.; Zhu, H.; Wang, Y.; Feng, W.; Hu, Y.; Dasgupta, A.; Han, Y.; Wang, Y.; Muller, D. A.; Martin, L. W.; et al. Intrinsic Two-Dimensional Ferroelectricity with Dipole Locking. *Phys. Rev. Lett.* **2018**, *120*, 227601.
(30) Hou, P.; Lv, Y.; Zhong, X.; Wang, J. α-In_2Se_3 Nanoflakes Modulated by Ferroelectric Polarization and Pt Nanodots for Photodetection. *ACS Appl. Nano Mater.* **2019**, *2*, 4443−4450.
(31) Shi, H.; Li, M.; Shaygan Nia, A.; Wang, M.; Park, S.; Zhang, Z.; Lohe, M. R.; Yang, S.; Feng, X. Ultrafast Electrochemical Synthesis of Defect-Free In_2Se_3 Flakes for Large-Area Optoelectronics. *Adv. Mater.* **2020**, *32*, 1907244−1907251.
(32) Yan, T.; Liu, F.; Wang, Y.; Yang, J.; Ding, C.; Cai, Y.; Wu, Z.; Zhan, X.; Wang, F.; Tian, Y.; et al. A Ferroelectric p−i−n Heterostructure for Highly Enhanced Short-Circuit Current Density and Self-Powered Photodetection. *Adv. Electron. Mater.* **2022**, *8*, 2101385.
(33) Jin, H. J.; Park, C.; Lee, K. J.; Shin, G. H.; Choi, S. Y. Ultrasensitive WSe_2/α-In_2Se_3 NIR Photodetector Based on Ferroelectric Gating Effect. *Adv. Mater. Technol.* **2021**, *6*, 2100494.
(34) Zou, J.; Ke, Y.; Zhou, X.; Huang, Y.; Du, W.; Lin, L.; Wei, S.; Luo, L.; Liu, H.; Li, C.; et al. Broadband Visible−Near Infrared Two-Dimensional WSe_2/In_2Se_3 Photodetector for Underwater Optical Communications. *Adv. Opt. Mater.* **2022**, *10*, 2200143.
(35) Zhu, C.; Wang, Y.; Wang, F.; Yang, J.; Zhan, X.; Fang, L.; Wang, Z.; He, J. Nonvolatile reconfigurable broadband photodiodes based on BP/α-In_2Se_3 ferroelectric p−n junctions. *Appl. Phys. Lett.* **2022**, *120*, 083101.
(36) Guo, H.; Xia, Y.; Yu, Y.; Zhou, R.; Niu, H.; Mao, X.; Wan, L.; Xu, J. High-speed and broadband spectral photodetectors based on β-In_2Se_3/Si heterojunction. *Materi. Sci. Semicon. Proc.* **2022**, *138*, 106304.
(37) Mech, R. K.; Mohta, N.; Chatterjee, A.; Selvaraja, S. K.; Muralidharan, R.; Nath, D. N. High Responsivity and Photovoltaic Effect Based on Vertical Transport in Multilayer α-In_2Se_3. *Phys. Status. Solidi. A* **2020**, *217*, 1900932.
(38) Chen, S.; Liu, X.; Qiao, X.; Wan, X.; Shehzad, K.; Zhang, X.; Xu, Y.; Fan, X. Facile Synthesis of gamma-In_2Se_3 Nanoflowers toward High Performance Self-Powered Broadband gamma-In_2Se_3/Si Heterojunction Photodiode. *Small* **2017**, *13*, 1604033.
(39) Guo, L.; Liu, X.; Cong, R.; Gao, L.; Zhang, K.; Zhao, L.; Wang, X.; Wang, R. N.; Pan, C.; Yang, Z. Patterned 2D Ferroelectric Perovskite Single-Crystal Arrays for Self-Powered UV Photodetector Boosted by Combining Ferro-Pyro-Phototronic and Piezo-Phototronic Effects. *Nano Lett.* **2022**, *22*, 8241−8249.
(40) Wan, S.; Li, Y.; Li, W.; Mao, X.; Zhu, W.; Zeng, H. Room-temperature ferroelectricity and a switchable diode effect in two-dimensional alpha-In_2Se_3 thin layers. *Nanoscale* **2018**, *10*, 14885−14892.
(41) Io, W. F.; Yuan, S.; Pang, S. Y.; Wong, L. W.; Zhao, J.; Hao, J. Temperature- and thickness-dependence of robust out-of-plane ferroelectricity in CVD grown ultrathin van der Waals α-In_2Se_3 layers. *Nano Res.* **2020**, *13*, 1897−1902.
(42) Lewandowska, R.; Bacewicz, R.; Filipowicz, J.; Paszkowicz, W. Raman scattering in α-In_2Se_3 crystals. *Mater. Res. Bull.* **2001**, *36*, 2577−2583.
(43) KüPers, M.; Konze, P. M.; Meledin, A.; Mayer, J.; Englert, U.; Wuttig, M.; Dronskowski, R. Controlled Crystal Growth of Indium Selenide, In_2Se_3, and the Crystal Structures of α-In_2Se_3. *Inorg. Chem.* **2018**, *57*, 11775−11781.
(44) Liu, L.; Dong, J.; Huang, J.; Nie, A.; Zhai, K.; Xiang, J.; Wang, B.; Wen, F.; Mu, C.; Zhao, Z.; et al. Atomically Resolving Polymorphs and Crystal Structures of In_2Se_3. *Chem. Mater.* **2019**, *31*, 10143−10149.
(45) Lv, B.; Yan, Z.; Xue, W.; Yang, R.; Li, J.; Ci, W.; Pang, R.; Zhou, P.; Liu, G.; Liu, Z.; et al. Layer-dependent ferroelectricity in 2H-stacked few-layer α-In_2Se_3. *Mater. Horiz.* **2021**, *8*, 1472−1480.
(46) Lipatov, A.; Sharma, P.; Gruverman, A.; Sinitskii, A. Optoelectrical Molybdenum Disulfide (MoS_2)–Ferroelectric Memories. *ACS Nano* **2015**, *9*, 8089−8098.
(47) Chen, Y.; Wang, X.; Huang, L.; Wang, X.; Jiang, W.; Wang, Z.; Wang, P.; Wu, B.; Lin, T.; Shen, H.; Wei, Z.; Hu, W.; Meng, X.; Chu, J.; Wang, J. Ferroelectric-tuned van der Waals heterojunction with band alignment evolution. *Nat. Commun.* **2021**, *12*, 4030−4038.
(48) Si, M.; Saha, A. K.; Gao, S.; Qiu, G.; Qin, J.; Duan, Y.; Jian, J.; Niu, C.; Wang, H.; Wu, W.; et al. A ferroelectric semiconductor field-effect transistor. *Nat. Electron.* **2019**, *2*, 580−586.
(49) Island, J. O.; Blanter, S. I.; Buscema, M.; van der Zant, H. S.; Castellanos-Gomez, A. Gate Controlled Photocurrent Generation Mechanisms in High-Gain In_2Se_3 Phototransistors. *Nano Lett.* **2015**, *15*, 7853−7858.
(50) Ahn, J.; Ko, K.; Kyhm, J. H.; Ra, H. S.; Bae, H.; Hong, S.; Kim, D. Y.; Jang, J.; Kim, T. W.; Choi, S.; et al. Near-Infrared Self-Powered Linearly Polarized Photodetection and Digital Incoherent Holography Using WSe_2/$ReSe_2$ van der Waals Heterostructure. *ACS Nano* **2021**, *15*, 17917−17925.
(51) Zhang, X.; Liu, X.; Zhang, C.; Peng, S.; Zhou, H.; He, L.; Gou, J.; Wang, X.; Wang, J. Epitaxial Topological Insulator Bi_2Te_3 for Fast Visible to Mid-Infrared Heterojunction Photodetector by Graphene As Charge Collection Medium. *ACS Nano* **2022**, *16*, 4851−4860.
(52) Xie, C.; Zeng, L.; Zhang, Z.; Tsang, Y.-H.; Luo, L.; Lee, J.-H. High-performance broadband heterojunction photodetectors based on multilayered $PtSe_2$ directly grown on a Si substrate. *Nanoscale* **2018**, *10*, 15285−15293.
(53) Liu, B.; Lyu, F.; Tang, B.; Li, X.; Liao, J.; Chen, Q. Contact Properties of Two-Dimensional Ferroelectric α-In_2Se_3. *ACS Appl. Electron. Mater.* **2021**, *3*, 4604−4610.
(54) Tang, W.; Zhang, X.; Yu, H.; Gao, L.; Zhang, Q.; Wei, X.; Hong, M.; Gu, L.; Liao, Q.; Kang, Z.; et al. A van der Waals Ferroelectric Tunnel Junction for Ultrahigh-Temperature Operation Memory. *Small Methods* **2022**, *6*, 2101583.
(55) Mukherjee, S.; Koren, E. Indium Selenide (In_2Se_3) − An Emerging Van-der-Waals Material for Photodetection and Non-Volatile Memory Applications. *Isr. J. Chem.* **2022**, *62*, 202100112.
(56) Wu, D.; Guo, C.; Zeng, L.; Ren, X.; Shi, Z.; Wen, L.; Chen, Q.; Zhang, M.; Li, X. J.; Shan, C.-X.; Jie, J. Phase-controlled van der Waals growth of wafer-scale 2D $MoTe_2$ layers for integrated high-sensitivity broadband infrared photodetection. *Light Sci. Appl.* **2023**, *12*, 5−17.

https://doi.org/10.1021/acsnano.2c11925
ACS Nano 2023, 17, 6534−6544